Nanoscale

PAPER

View Article Online
View Journal

Cite this: DOI: 10.1039/d6nr00051g

Structurally robust quaterphenyl-dicarbonitrile 2D MOF nanopores on Cu(111) for cobalt spin-coordination motifs

Haruki Ishii,[a] Kohei Tada,[b,c] Ryo Ichikawa,[a] Meng-Che Tsai,[d] Kuei-Cheng Chen,[d] Ryunosuke Sagehashi,[e] Fumi Nishino,[e] Keisuke Fukutani,[e] Rikuya Hirota,[b] Yasutaka Kitagawa,[b,c] Satoshi Kera,[e] Masaki Horie[d,f] and Toyo Kazu Yamada *[a,g]

We demonstrate a strategy for fabricating robust ~2 nm nanopores on copper (Cu) surfaces using a non-magnetic two-dimensional (2D) metal–organic framework (MOF), without the need for additional 3d metal atom deposition, that serves as a platform for constructing single-atom transition-metal coordination sites. Scanning tunneling microscopy and spectroscopy (STM/STS) conducted at 78 K under ultra-high vacuum (UHV), along with angle-resolved photoemission spectroscopy (ARPES) at 300 K, provide direct insight into the electronic structure. Machine-learning interatomic potential (MLIP) calculations and density functional theory (DFT) further evaluate the energetic stability of the system. Deposition of the molecular precursor [1,1′′:4′,1′′:4′′,1′′′-quaterphenyl]-4,4′′′-dicarbonitrile (Ph_4DN) onto Cu(111) results in a quasi-honeycomb 2D MOF stabilized by Cu adatoms. In contrast to the analogous MOF on Ag(111), which requires additional 3d metal atom linkers to form a 2D MOF, and where excess 3d atoms beyond the stoichiometric ratio disrupt the MOF's regularity, the Cu-supported MOF remains intact, reflecting stronger MOF-substrate interactions on Cu(111). The reduced mobility of molecular species on Cu(111) leads to the coexistence of 2D MOF, 1D MOF, and self-assembled monolayer domains, with the 2D MOF being the most energetically favorable. Focusing on the electronic structure of the 2D MOF on Cu(111), we show that its nanopores serve as stable confinement sites that can trap conduction electrons, leading to the formation of quantum-well states, while also accommodating additional precursor molecules and Co atoms without forming chemical bonds. These capabilities suggest that the nanopores function as nanoscale reactors capable of assembling diverse coordination motifs. This approach offers a versatile strategy for engineering well-defined nanopores within nonmagnetic 2D MOFs, capable of hosting isolated atoms and molecules, and provides promising opportunities for applications in single-atom electronics, spintronic devices, quantum materials, and catalytic platforms.

Received 6th January 2026,
Accepted 14th April 2026

DOI: 10.1039/d6nr00051g

rsc.li/nanoscale

1. Introduction

Engineering nanopore arrays with 2 nm dimensions on a solid surface using two-dimensional (2D) honeycomb-structured covalent organic frameworks (COFs)[1–17] or metal–organic frameworks (MOFs)[18–32] holds significant promise as an advanced platform for constructing transition-metal coordination motifs.[33–37] In such systems, individually coordinated atoms can exhibit quantum spin states, making them promising candidates for quantum materials used in sensors, qubits, and quantum dots, namely corresponding to on-surface engineering of single-atom magnets, similar to single molecular magnets.[38–55] Moreover, if the centrally coordinated atom acts as a catalytic site, each 2 nm nanopore can serve as a nanoreactor, enabling single-atom catalysis.[56–58]

[a]Department of Materials Science, Chiba University, 1-33 Yayoi-Cho, Inage-ku, Chiba 263-8522, Japan. E-mail: toyoyamada@faculty.chiba-u.jp
[b]Department of Materials Engineering Science, Graduate School of Engineering Science, The University of Osaka, Toyonaka, Osaka 560-8531, Japan
[c]Innovative Catalysis Science Division, Institute for Open and Transdisciplinary Research Initiatives (ICS-OTRI), The University of Osaka, Suita, Osaka 565-0871, Japan
[d]Department of Chemical Engineering, National Tsing Hua University, 101, Sec. 2, Kuang-Fu Road, Hsinchu, 30013, Taiwan
[e]Institute for Molecular Science, Myodaiji, Okazaki 444-8585, Japan
[f]Research Institute for Electronic Science, Hokkaido University, N21W10, Kita-Ward, Sapporo 001-0021, Japan
[g]Molecular Chirality Research Centre, Chiba University, 1-33 Yayoi-cho, Inage-ku, Chiba 263-8522, Japan

The formation of 2D COF on noble metal surfaces such as Au, Ag, and Cu typically relies on a thermally activated Ullmann coupling reaction.[1–17] In this process, precursor molecules terminated with halogen atoms (*e.g.*, Br, Cl, or I) are first adsorbed onto the surface. Subsequent annealing cleaves the halogen atoms from the precursors, while thermal diffusion promotes covalent bonding between the precursor units, leading to the formation of a supramolecular network. However, the Ullmann reaction often proceeds through unstable intermediate states,[59–61] which can compromise the structural integrity of the resulting nanopores.

In contrast, the synthesis of 2D MOF does not require Ullmann reaction, and the precursor molecules therefore do not need to be halogen-terminated. Instead, the precursors adsorb and coordinate with surface adatoms, typically adopting a C_3-symmetric configuration that leads to the formation of a honeycomb lattice.[18–32] Adatoms of Au, Ag, and Cu have been studied as coordination centers in such frameworks.[62–66] To date, relatively simple molecular structures, such as linear benzene-ring sequences or trisubstituted benzenes terminated with nitrile (–CN) groups, have been primarily investigated.[64–67] In addition, because 2D MOFs and COFs can confine surface-state electrons within nanoscale pores, the behavior of quantized electrons in these systems has been actively investigated.[32,66,68]

However, for such nanopores to function practically as traps not only for electrons but also for guest atoms and molecules, the structural robustness of the host framework is essential. For example, when using precursors terminated with nitrile (–CN) groups, deposition on Ag or Au substrates alone typically yields a self-assembled monolayer (SAM) rather than a 2D MOF, due to the weak interaction between the substrate and the precursors.[64] The formation of a well-ordered 2D MOF on these substrates generally requires the addition of 3d transition metal atoms (*e.g.*, Co, Fe, or Ni) as linkers. Furthermore, precise control of stoichiometry is essential: a uniform 2D MOF forms when the number of 3d metal atoms matches that of the precursor molecules, whereas excess metal atoms readily disrupt the structural regularity of the MOF.

Consequently, to date, most 2D MOFs on Ag or Au substrates require 3d transition-metal atoms to link precursor molecules, due to the relatively weak substrate–precursor interactions. This often results in ferromagnetic 2D MOFs,[69,70] which can limit the use of nanopores for designing new 3d-atom-based coordination motifs.

In contrast, we show that a nonmagnetic 2D MOF on Cu(111) serves as a robust template for constructing the desired 3d-atom coordination motifs. Although 2D MOFs on Cu(111) have been demonstrated,[67] previous studies have primarily focused on quantum confinement of surface-state electrons within the nanopores. As a result, the intrinsic electronic structure of the 2D MOF itself, as well as whether the adsorption of additional 3d atoms at 300 K modifies the 2D MOF, remains largely unexplored.

The nanopores are formed within a 2D MOF composed of [1,1″:4′,1″:4″,1‴-quaterphenyl]-4,4‴-dicarbonitrile (Ph_4DN) molecules assembled on an atomically flat Cu(111) substrate, without the need for additional 3d metal atom deposition. On Cu(111), Cu adatoms coordinate with Ph_4DN in a C_3-symmetric manner, generating a quasi-honeycomb lattice. Importantly, Cu adatoms significantly enhance the structural robustness of the MOF: the 2D nanopore architecture remains intact after Co deposition. Notably, no structural changes are observed in the 2D MOF on Cu(111) following Co deposition at 300 K, enabling the formation of a Co–Ph_4DN coordination motif within the nanopores. Thus, we demonstrate the successful realization of this coordination structure.

Scanning tunneling microscopy and spectroscopy (STM/STS) measurements were conducted at 78 K under ultrahigh-vacuum (UHV) conditions, and angle-resolved photoemission spectroscopy (ARPES) and X-ray photoelectron spectroscopy (XPS) measurements were performed at 300 K in UHV. Machine-learning interatomic potential (MLIP) calculations combined with density functional theory (DFT) were used to evaluate the energetic stability of the system.

2. Methods

2.1 Home-built low-temperature UHV STM setup

The experiment was performed with a home-built low-temperature STM at 5 K under UHV. The setup consists of the introduction, preparation, and analytical chambers with the base pressure below 10^{-8} Pa.[71–73] A UHV cryostat (CryoVac), including an outer liquid nitrogen tank (15 liters) and an inner helium tank (8 liters), is docked in the analytical chamber. The STM was placed at the center of the analytical chamber and thermally contacted with the cryostat. Heat radiation from the analytical chamber to the STM was cut with two cylindrical cooling shields, which maintained the STM temperature at 78 K for more than 80 h.

2.2 STM/STS measurements

STM and scanning tunneling spectroscopy (STS) measurements were performed with a combined Nanonis SPM controller and software. The topographic images were obtained in a constant current mode. STS was done by measuring tunneling current as a function of sample bias voltage ($I(V)$) at each pixel position in an STM topographic image (feedback-off grid mode). Differential conductance (dI/dV) curves, which are proportional to the sample local density of states (LDOS), were obtained using WSxM 5.0 Develop 10.0 software[74] *via* numerical differentiation of $I(V)$ by the sample bias voltage (V). The dI/dV spectra were normalized by tunneling probability function (T) using Microsoft Excel to obtain the $(dI/dV)/T$ curve.[75,76] These STM and STS measurements were performed on multiple independently prepared samples, and the characteristic structural and electronic features were reproducibly observed across different sessions.

2.3 Fabrication of W tip

STM tips were fabricated from polycrystalline W and Mo wires with a diameter of 0.3 mm (purity 99.95%) *via* electrochemical

etching using KOH aq.[77] as well as the flame-etching process[78,79] and subsequently transferred into the UHV preparation chamber. Then, the tip apex was flashed at 2000 K to exclude oxide layers.[77] The cleaned tip was again transferred to the UHV analytical chamber without breaking UHV and set into the STM using a wobble stick. STM topographic images alone do not provide detailed information on whether Co adsorption leads to the formation of new chemical bonds with the 2D MOF. In this study, we therefore focus on obtaining stable spectroscopic data, using relatively blunt tips to ensure reliable STS measurements.

2.4 Cu(111) substrate

The Cu(111) single crystal (diameter 6 mm, MatecK, purity 99.9999%) was cleaned through repeated cycles of Ar^+ sputtering (+1 kV, 500 nA) and annealing (873 K) in a UHV environment (SI, Fig. S1). Atomically flat terraces separated by the monolayer height steps (step defects) give a terrace width ranging from 50 to 100 nm with an impurity level below 1%.

2.5 UHV molecule sublimation

The synthesized Ph_4DN molecules were first characterized by using ^1H NMR spectroscopy (Bruker 500 MHz spectrometer) and field-desorption mass spectrometry (JEOL JMS-T200GC AccuTOF GCX) (SI, Fig. S2). The molecules were then placed in a quartz crucible and sublimated in the preparation chamber (pressure below 3.0×10^{-7} Pa) by radiative heating (SI, Fig. S3). The crucible temperature was monitored using the alumel–chromel thermocouple directly in contact with the crucible and maintained at 373 K. The deposition amount of Ph_4DN was controlled by a quartz crystal microbalance (QCM) (parameters: *z*-ratio = 1.00, density = 1.00).[73] Then, we deposited an amount of Ph_4DN molecules, approximately 0.19 nm thickness, onto the cleaned Cu(111) surface at 300 K in UHV. STM topographic images confirmed that this 0.19 nm thickness provides an approximately one monolayer coating of Ph_4DN on Cu(111).

2.6 Cobalt deposition

A coverage of 0.01 monolayers (ML) of cobalt (Co), corresponding to 2–3 atoms confined within each nanopore of the 2D-MOF, was deposited from an electron bombardment-type evaporator using a Co rod (diameter: 2.0 mm, purity: 99.99%, Nilaco) at a sample temperature of 300 K under UHV conditions. The deposition rate was monitored with a QCM (parameters: *z*-ratio = 1.37, density = 8.90). This atomically precise deposition enables precise control over the placement of 3d-transition-metal atoms on a surface.[80]

2.7 Angle-resolved photoemission spectroscopy and X-ray photoelectron spectroscopy

All angle-resolved photoemission spectroscopy (ARPES) measurements were performed at 300 K in UHV below 1×10^{-8} Pa, equipped with a hemispherical electron energy analyzer (MBS A-1) and twin monochromators (MBS TM-1) for two wavelength regions (SI, Fig. S4).[81] He-Iα radiation ($h\nu$ = 21.218 eV) was used as the excitation source. The Ph_4DN molecules were sublimated in the UHV deposition chamber (below 6×10^{-8} Pa) under the same conditions as in the STM experiments. X-ray photoelectron spectroscopy (XPS) measurements were also performed at 300 K with Al-Kα radiation ($h\nu$ = 1486.6 eV) in UHV below 1×10^{-8} Pa, equipped with a hemispherical electron energy analyzer (SI, Fig. S5).

2.8. Computational procedure

The geometric structures and total energies of 2D MOFs on Cu (111) were calculated by MLIPs.[82] The MLIP used is the Preferred potential (PFP), which is proposed as a universal potential using graph neural networks.[83] The used version and mode of PFP were v6.0.0 and CRYSTAL U0 PLUS D3, respectively. *Ab initio* band calculations based on DFT were used to validate the prediction accuracy of the PFP. The comparison of the geometry optimization results for the 2D MOF model without a Cu substrate showed that PFP gave a similar converged structure to DFT and consistent values for the atomic charge of copper in the metal center (SI, Fig. S6). In addition, the results of PFP and DFT calculations were compared with respect to energy dependence on the distance between the Cu substrate and 2D MOF; as shown in the calculated results (SI, Fig. S7), the calculated energy by PFP has good agreement with that by DFT. From these results, we assumed that 2D MOF calculations by PFP would have the same accuracy as DFT calculations of the systems. The details of the comparison of DFT and PFP are depicted in the SI Note 1 and Fig. S6 and S7.

3. Results and discussion

To construct a secondary 2D coordination network within the nanopores of the existing 2D MOF, it is crucial to assess whether the Cu-adatom–coordinated framework is robust enough to withstand the adsorption of reactive 3d-transition-metal atoms (Fig. 1a). This assessment is crucial, as previous studies have shown that 2D MOFs constructed with 3d metal linkers (*e.g.*, Fe or Co) on Ag substrates are readily destabilized by additional Co adsorption. This instability arises from the relatively weak interaction between the Ag surface and the –CN groups of Ph_4DN, in contrast to the stronger Co–Ph_4DN coordination.[64]

In contrast, as illustrated in the right panel of Fig. 1a, the 2D MOF formed on a Cu substrate exhibits significantly stronger coupling between the terminal nitrogen atoms of the Ph_4DN molecules and the Cu adatoms. This enhanced stability originates from electronic hybridisation between Cu and N orbitals, which reinforces the framework against structural disruption.

Here, we investigate the robustness of this 2D MOF on Cu (111) against additional Co deposition at 300 K. If no new electronic bonds form *via* decoupling of the Cu–N interactions, Co deposition will not disrupt the original 2D MOF. Under these conditions, if more than two Co atoms occupy a single nanopore, they can rapidly aggregate to form nanoclusters, similar to the Co nanocluster formation observed in COFs on Cu (111).[16] Alternatively, when a Co atom encounters Ph_4DN molecules within a nanopore, Co–Ph_4DN coordination may form.

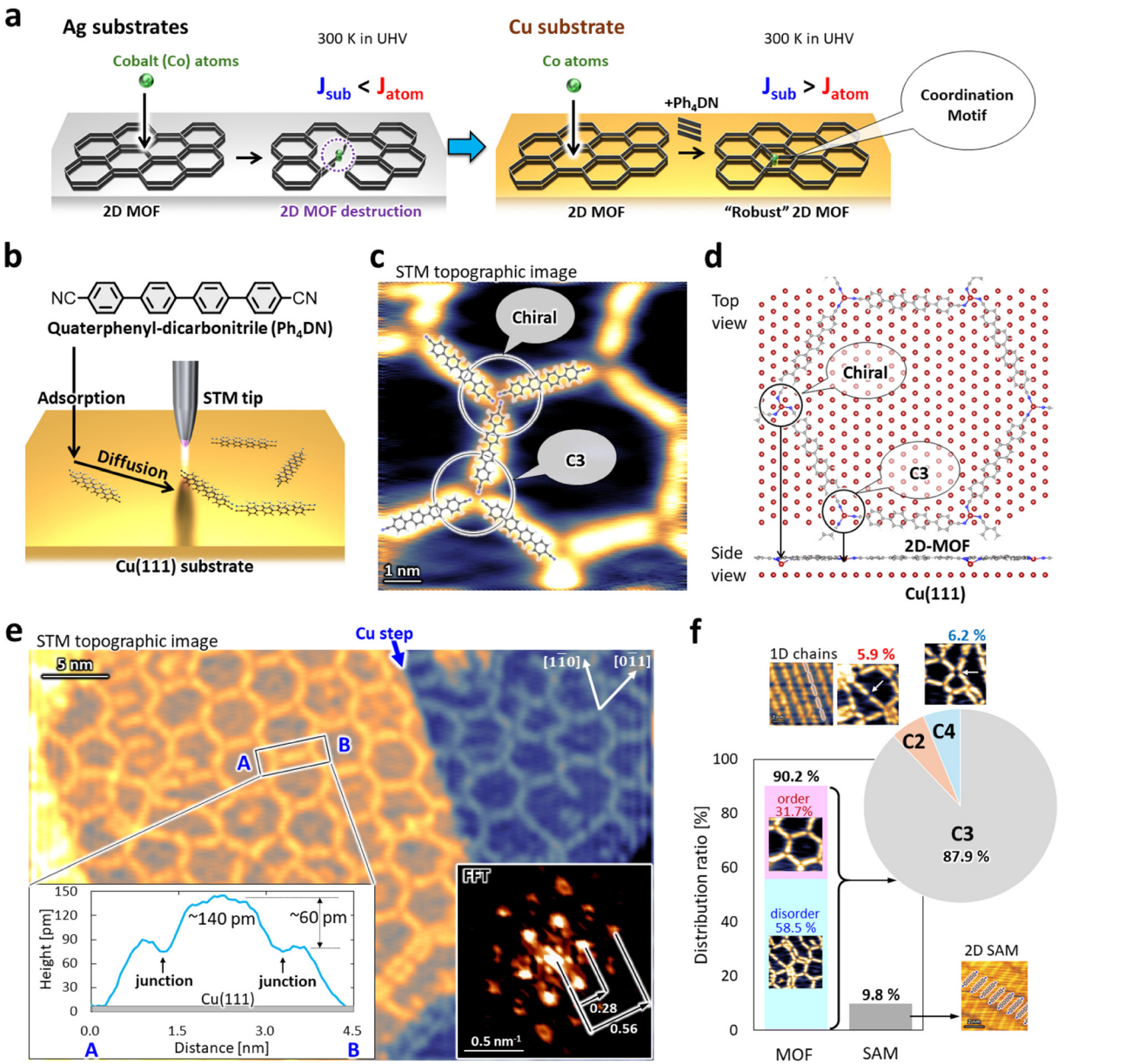

Fig. 1 (a) Schematic models of Co-atom adsorption on a 2D MOF fabricated on Ag (left) and Cu (right) substrates. The structural robustness of the 2D MOF is governed by the balance between the interactions originating from the substrate (J_{sub}) and those associated with the adsorbed Co atom (J_{atom}). (b) Schematic model illustrating the STM tip scanning at 78 K in UHV on the Cu(111) surface with Ph_4DN absorption. (c) Magnified STM topographic image showing C_3 symmetric and chiral coordination motifs (7.2 × 7.2 nm^2, V_s = −1.0 V, I_t = 50 pA). (d) MLIPs optimized structural model corresponding to the STM image in (c). (e) Large-area STM topographic image (48 × 32 nm^2, V_s = 750 mV, I_t = 50 pA) demonstrating that the carpet-like 2D MOF film extends continuously across Cu step edges. Lower-left inset: height profile measured along the A–B line. Lower-right inset: FFT map revealing six-fold symmetric spots with two distinct periodicities. Right panel: inverse FFT image (39 × 44 nm^2) where terraces of varying height are normalized to a single level, highlighting the hidden Cu step edges (indicated by blue arrows). (f) Distribution ratio of the total surface area after the Ph_4DN deposition on Cu(111) at 300 K in UHV, where 90.2% of the Cu(111) surface is covered by the MOF, including C_2 (5.9%), C_3 (87.9%), and C_4 (6.2%) coordination, while the remaining 9.8% was covered by the 2D SAM array.

Moreover, for applications in quantum technologies, it is desirable that the adsorbed metal atoms possess electronic spin. Given that Ph_4DN molecules are also present in the coordination environment, we performed DFT calculations to predict the charge and spin states of Co and Fe adatoms within Ph_4DN-based coordination fields. The computational conditions and results are summarized in SI, Fig. S8. The calculations reveal that none of the metal adatoms exhibit a singlet (S = 0) ground state. Notably, the S = 1/2 spin state, considered essential for realizing Kitaev quantum spin liquids,[84] was found to be energetically favorable for Co adatoms, particularly at lower oxidation states compared to Fe, when co-

ordinated by Ph_4DN. These findings motivated our focus on Co adsorption onto the 2D MOF structure. Therefore, it is desirable for the 2D MOF itself to be nonmagnetic, exhibiting negligible spin.

In this study, we employed the precursor Ph_4DN, a molecule composed of four benzene rings terminated with nitrile (–CN) groups (see Fig. 1b). This choice was motivated by our initial attempt to use a shorter linear precursor, 1,4-di(4-pyridyl)benzene (DPB), on Cu(111), which did not yield a well-ordered 2D MOF (SI, Note 2 and Fig. S9). Ph_4DN sublimated reproducibly at a crucible temperature of 373 K under UHV conditions, enabling the formation of a quasi-honeycomb 2D MOF with a nanoporous structure on the Cu(111) substrate. In this network, Cu adatoms likely acted as coordination centers.

3.1 Growth of 2D-MOF on Cu(111) surface

Ph_4DN precursor molecules were deposited onto a clean, atomically flat Cu(111) surface at 300 K under UHV conditions, as illustrated by the model in Fig. 1b. The sample was subsequently transferred to the analysis chamber without breaking the UHV environment, and STM/STS measurements were conducted at 78 K under UHV. A 2D MOF forms on the Cu (111) surface due to coordination between the terminal nitrile (–CN) groups and Cu adatoms supplied by the substrate.

Fig. 1c shows an STM topographic image of the resulting 2D-MOF on Cu(111), where the linear Ph_4DN molecules appear as bright lines, and the Cu(111) substrate appears as a dark-blue background. Hexagonally shaped nanopores are clearly observed. Molecular models suggest that the side length of each hexagonal nanopore corresponds to the length of a single Ph_4DN molecule, resulting in a periodic nanopore array with an approximate nanopore size of 2 nm. In the STM image, the junctions where three Ph_4DN molecules meet appear as darker spots with lower apparent height, indicating the presence of a Cu adatom situated between the Cu(111) surface and the molecules. Initially, we assumed that the resulting 2D network possessed perfect honeycomb symmetry. However, the STM topography shown in Fig. 1c clearly reveals that the network consists of two distinct types of coordination. In the first type, Ph_4DN molecules are arranged with C_3 symmetry, extending in three directions at 120° intervals, around the junction ("C_3" in Fig. 1b). In the second type, although the Ph_4DN molecules are also oriented at approximately 120° angles, the junction is slightly offset from the molecular axis, giving rise to a chiral coordination geometry around the Cu center ("chiral" in Fig. 1c), similar to that observed for NC–Ph5–NC on Cu(111).[67]

To gain deeper insight into the 2D-MOF formation on Cu (111), we performed MLIP calculations. The optimized structure obtained from the MLIP calculation is shown in Fig. 1d, successfully reproducing both the C_3-symmetric and chiral coordination motifs observed in the STM images. The calculation started from an ideal honeycomb configuration, yet the resulting optimized structure converged into a quasi-honeycomb arrangement, consistent with experimental observations. Furthermore, the MLIP results suggest that the junction may involve a Cu adatom originating from the Cu(111) subsurface; in other words, the Cu adatoms are likely not coplanar with the Ph_4DN molecules. The emergence of chirality appears to be independent of specific adsorption sites on the Cu surface, suggesting that the stabilization provided by coordination bonding outweighs the energy preference for site-specific adsorption of the Cu adatoms. Importantly, we were unable to obtain a stable 2D structure in the absence of the Cu substrate. Optimized structures without the Cu(111) surface showed significant distortions and torsions in the Ph_4DN molecules, leading to three-dimensional geometries (see SI, Fig. S6). These findings indicate that the formation of the 2D structures described in this study is strictly surface-assisted and cannot occur in the absence of the substrate.

The wide-area STM topographic image shown in Fig. 1e provides a key insight: the 2D-MOF composed of Cu adatoms and Ph_4DN molecules is capable of spanning Cu step edges, enabling the formation of a continuous, ordered nanopore network across the surface. In the image, the network is not perfectly ordered; it contains distortions and non-ideal hexagonal features. However, the network pattern appears to match seamlessly across adjacent terraces, suggesting that the coordination framework bridges the atomic steps. The inset in the lower left of Fig. 1e shows a height profile taken along the line between points A and B in the main image. This profile reveals that an individual Ph_4DN molecule exhibits a height of approximately 140 pm and a length of ~2 nm, in good agreement with theoretical predictions shown in Fig. 1d. Additionally, the Cu adatom appears ~60 pm lower in apparent height than the Ph_4DN molecule, suggesting that it resides between the Ph_4DN and the Cu(111) surface, partially embedded in the substrate plane. The STM data thus indicate a Cu adatom height of approximately 80 pm above the surface.

To examine the periodicity of the coordination network in more detail, we analyzed a fast Fourier transform (FFT) map shown in the lower right inset of Fig. 1e. This map reveals sixfold-symmetric spots at 0.28 nm^{-1} and 0.56 nm^{-1}, corresponding to the first- and second-order reflections of the honeycomb structure. These FFT features indicate that the quasi-honeycomb network is epitaxially aligned with the Cu(111) surface, specifically along the $[1\bar{1}0]$ and $[0\bar{1}1]$ crystallographic directions. The unit cell periodicity is determined to be approximately 3.57 nm. The degree of epitaxial registry between the molecular network and the underlying Cu(111) substrate can be quantitatively evaluated using the phase match rate (PMR), defined as PMR [%] = 100 $(1 - |b - na|/b)$, where a is the atomic lattice constant of Cu(111) (0.256 nm), b is the periodicity of the molecular network (3.57 nm), and n is an integer chosen to minimize the lattice mismatch. Substituting n = 14 yields a PMR of 99.61%, indicating an almost perfectly commensurate relationship. This high degree of lattice matching suggests that the growth of the honeycomb structure is strongly influenced by the threefold symmetry of the Cu(111) surface, which promotes the formation of an ordered molecular network. In summary, the Ph_4DN-based honeycomb structure coordinated on the Cu surface exhibits

both strong molecule–substrate interactions, as evidenced by the high PMR and epitaxial alignment, and inherent structural robustness, enabling it to span step edges and surface defects without loss of structural integrity.

However, it should be noted that the strong interaction with the substrate (J_{sub}) significantly restricts the mobility of the precursors on the Cu surface, thereby reducing the uniformity of the resulting MOF. Under deposition conditions of 300 K in UHV, Ph_4DN molecules form not only the dominant quasi-honeycomb 2D MOF with C_3 symmetry (84.9%), but also a 1D chain-like structure with C_2 symmetry (5.3%) and self-assembled monolayer (SAM) arrangement (9.8%), as shown in Fig. 1f and also SI, Fig. S10–S13. These statistics suggest that C_3 coordination is likely the most energetically favorable configuration; however, the well-ordered honeycomb 2D MOF covers only 28.6% of the surface.

Based on our STM experiments, we gained insights into improving the regularity of the 2D MOF. We compared two STM conditions (see SI, Fig. S14): (i) Ph_4DN deposited on Cu (111) at 300 K, held for 10 min, then cooled to 78 K; and (ii) deposition at 300 K followed by immediate cooling. Although both conditions yield MOF formation, pronounced SAM regions are observed only in the latter case, indicating that thermal energy promotes MOF formation. Accordingly, improving MOF regularity at 300 K can be achieved by using a slower deposition rate, maintaining the substrate at 300 K, or applying mild post-deposition annealing before cooling.

3.2 Electronic-structure insights into a 2D MOF on Cu(111)

Adsorption of Ph_4DN molecules onto the Cu(111) surface at 300 K under UHV conditions leads to the formation of a robust quasi-honeycomb 2D MOF carpet. This structure exhibits ~2 nm-sized nanopores with a unit-cell periodicity of ~3.57 nm, providing a promising platform for advanced coordination chemistry, including the selective trapping of Co atoms. As a first step toward this application, we deposited additional Ph_4DN molecules onto the preformed nanopore array (Fig. 2a).

Initially, it was also unclear whether the extra Ph_4DN molecules were successfully trapped within the nanopores, as individual molecules can thermally diffuse even at 78 K. However, by carefully tuning the bias voltage and employing differential conductance (dI/dV) mapping, we were able to confirm the presence of diffusing molecules inside the nanopores. The left panel of Fig. 2b shows an STM topographic image of the honeycomb nanopore array, where nanopores of two apparent heights coexist, appearing as bright and dark regions. Identification of the nanopore types was achieved using the simultaneously acquired dI/dV map at −0.24 V, shown in the right panel of Fig. 2b. In this map, the bare Cu(111) nanopores appear as bright spots, while both the fixed Ph_4DN molecules of the 2D MOF network and the diffusing Ph_4DN molecules within the nanopores appear darker. This contrast arises because Ph_4DN molecules possess a HOMO centered around −2.4 eV (Fig. 2e), far below the Fermi level, resulting in reduced electronic states near −0.24 V.

Averaged dI/dV spectra acquired over the unfilled nanopores of the 2D MOF (black line) and over Ph_4DN molecules (blue and red lines) were normalized using the tunneling probability function (T) to extract the local density of states (LDOS) of the sample,[75,85] as shown in Fig. 2c. Within the nanopores, quantized Cu(111) surface states give rise to several LDOS peaks near the Fermi energy. dI/dV maps obtained over the honeycomb domain (SI, Fig. S13) reveal spatially resolved electronic features. At a bias of −0.50 V, the periodic contrast of the honeycomb network is clearly visible, indicating reduced LDOS in the molecular framework compared to the bare Cu(111) surface, as also shown in Fig. 2c. At biases of −0.20 V, +0.50 V, and +0.75 V, enhanced LDOS signals are observed at the centers of the nanopores, forming a periodic array. These features are consistent with quantum confinement effects of the Cu(111) surface-state electrons within the nanopores. Such spatially confined states, commonly referred to as quantum corrals,[68,86,87] are known to produce discrete resonance peaks at multiple energy levels, in agreement with the LDOS peaks observed in our measurements.

In the STS measurements shown in Fig. 2b and c, no Cu–N bonding states were observed at the linker positions near the Fermi energy (also no significant changes in XPS measurements: SI, Fig. S5). To further investigate, we performed DFT calculations examining the bonding between Cu adatom linkers and the terminal N atoms of Ph_4DN. For the C_3 junction, bonding arises *via* Cu 3d and N 2p orbital hybridisation, while for the chiral junction, hybridisation occurs between Cu 4s and N 2s orbitals (SI, Fig. S15). The calculated results show that the chiral junction is less stable than C_3 junction because the hybridisation peak of Cu 4s and N 2s orbitals is in higher energy region than that of Cu 3d and N 2p orbitals. Interestingly, these hybridized states are located far below the Fermi energy, indicating the robustness of the Cu–Ph_4DN coordination.

Fig. 2d provides additional ARPES evidence showing that the Cu(111) surface feature disappears following Ph_4DN deposition. No new peaks emerge near the occupied states, indicating that the clean surface hosts a Shockley-type surface state (not shown in the ARPES spectra), which vanishes after molecular adsorption. In contrast, all Ph_4DN molecules, whether arranged in the 2D MOF, 1D chain, or SAM structures, exhibit a broad LDOS peak in the range of 0.5–1.0 V, which could be attributed to the lowest unoccupied molecular orbital (LUMO) of Ph_4DN.

Notably, the quasi-honeycomb 2D MOF film exhibits a broad band feature in k-space, despite structural imperfections and local disorder. Fig. 2e shows ARPES results for the bare Cu (111) surface (left panel) and for surfaces coated with Ph_4DN at thicknesses of 0.15 nm (center panel) and 4 nm (right panel), all displayed in second-derivative mode to enhance spectral contrast (ARPES spectra at various emission angles are provided in SI, Fig. S4). These ARPES maps represent the spatially averaged electronic structure of the sample surfaces. The pristine Cu(111) surface displays the *s*p band and five 3d bands, labeled 1–5. The second-derivative ARPES map of the clean surface clearly shows the *sp* band and the 3d bands.[88]

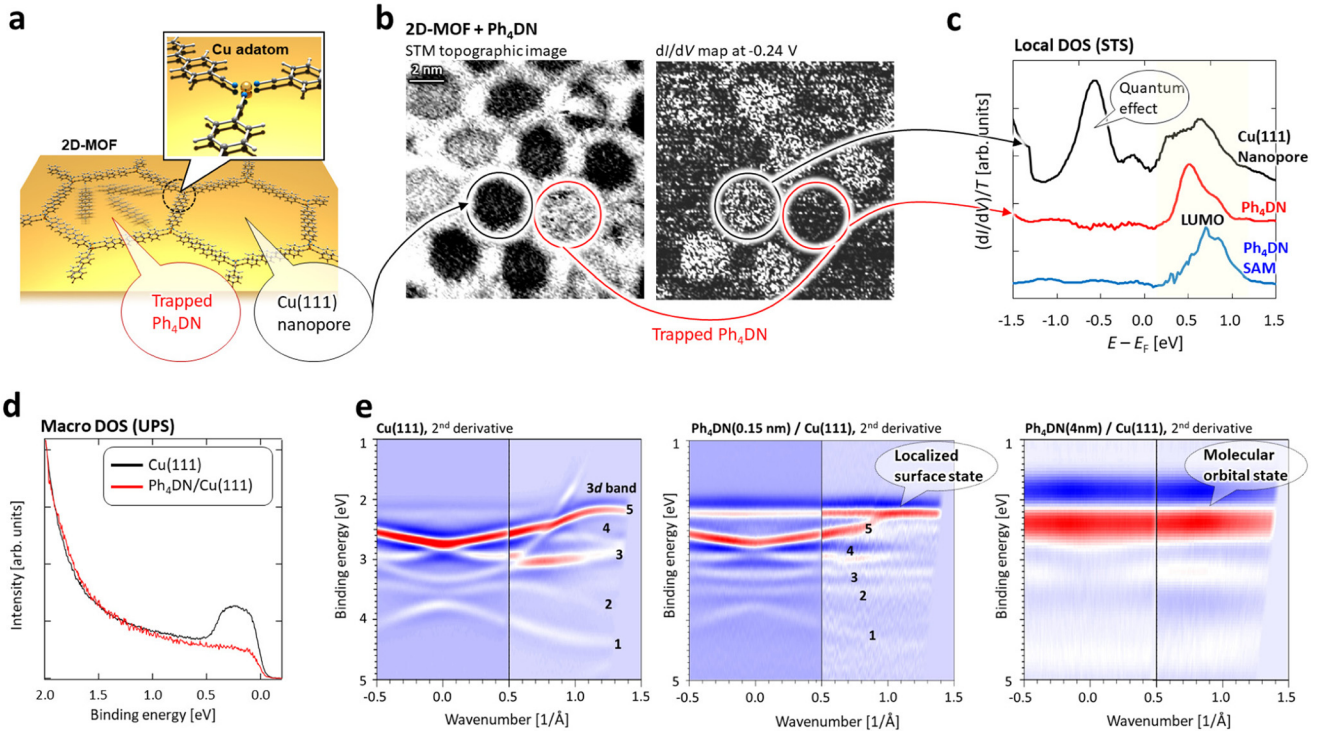

Fig. 2 (a) Schematic model of the Ph_4DN 2D-MOF coordinated on the Cu(111) surface. (b) Left panel: STM topographic image of the $[Ph_4DN–Cu]_3$ coordination network on Cu(111) (14 × 14 nm^2, V_s = −750 mV, I_t = 50 pA). Right panel: simultaneously obtained d*I*/d*V* map at −0.24 V. (c) Normalized differential conductance spectra: (d*I*/d*V*)/*T* curves, representing the sample LDOS, obtained at different locations: on Cu(111) nanopores (black), on a Ph_4DN molecule within the coordination network (red), and on a Ph_4DN molecule in a SAM array (blue). (d) Angle-integrated UPS spectra of the Cu (111) surface before and after deposition of Ph_4DN molecules. (e) The second-derivative intensity maps of ARPES results of the bare surface and the surface after Ph_4DN deposition of 0.15 nm and 4 nm.

For 0.15 nm Ph_4DN on Cu(111), the Cu-derived *sp* band disappears and the 3d-derived bands show slight modifications, with no distinct features attributable to Ph_4DN. The present ARPES experiments do not give evidence for the significant impacts of a charge localization on the Shockley surface state near the Fermi level, as found in the STS and the previous ARPES studies.[68] On the other hand, another surface state derived from Cu 3d orbital located at $k \sim 1.0$–1.5 Å^{-1} and the binding energy of ~2.2 eV on Cu(111), called a Tamm surface state,[89] shows flattening after the deposition of 0.15 nm of Ph_4DN. Such a modification may be attributable to the hybridisation of the Tamm surface state on Cu(111) to the molecular orbitals, leading to the nearly dispersionless (*i.e.*, localized) surface state induced by the MOF formation. For 4.0 nm Ph_4DN on Cu(111), the ARPES map reveals a broad band feature at approximately 2.2–2.6 eV, which is associated with bulk-like molecular orbital states of the film.

A similar trend of band-flattening (*i.e.*, enlargement of the electron effective mass) is also found for the 3d bands 2 and 3. The electron localization of surface atoms could be caused by the hybridisation between the 3d states and the molecular orbital states. Although the interaction is not expected to be strong enough to bring Cu-surface reconstruction, the impacts of the proper matching of each energy level on the hybridisation is realized. The results of hybridized interface states suggest that the decoupling effect of Co atoms from the Cu 3d electrons could be controlled by proper arranging of the overlayer materials (though the detailed discussion is hardly performed for the averaged ARPES data).

3.3 Co adsorption on 2D SAM and MOF supported on Cu(111)

To further evaluate the coordination strength between Ph_4DN molecules and Co atoms, we investigated how Co deposition influences the structural integrity of the 2D SAM film (Fig. 3a and SI, Fig. S13 and S14). Fig. 3b and c show STM images acquired within the SAM interior and at the SAM edges, respectively, after Co deposition. These observations indicate that the Ph_4DN–Co interaction (J_{Co}) is stronger than both the intermolecular interactions within the SAM and the interaction between the SAM and the Cu substrate (J_{sub}). Consequently, individual Ph_4DN molecules energetically favor breaking away from the original SAM array to connect *via* Co atoms. In most cases, the Co atoms appear to coordinate with Ph_4DN molecules in a C_3 symmetric manner. Supporting this, DFT calculations shown in SI, Fig. S8 suggest that the Co atom can possess a spin state of S ~ 1/2, consistent with the C_3 coordination.

However, the adsorption of Co atoms on the 2D MOF nanopores exhibits different behavior, as shown in Fig. 3d–f. This is because the interaction between the Cu substrate and the 2D

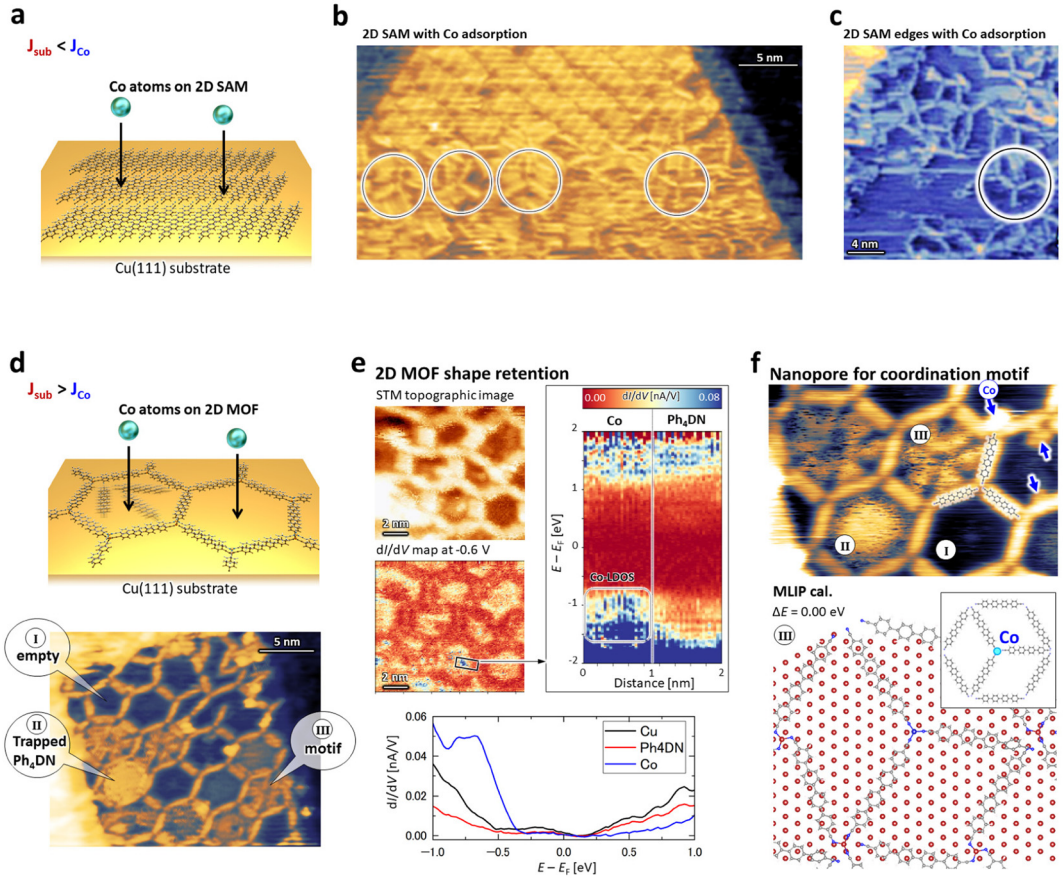

Fig. 3 Co atom adsorption, with a coverage corresponding to approximately one Ph_4DN molecule per 2.4 × 2.4 nm^2. (a) Schematic model of the Co-atom adsorption on the Ph_4DN SAM/Cu(111). (b) STM topographic image of the Ph_4DN SAM array region on Cu(111) after Co atom deposition (35 × 17 nm^2, 20 pA, −1.8 V). (c) STM topographic image of Co atom adsorbed on the Ph_4DN SAM edge region (24 × 24 nm^2, V_s = −750 mV, I_t = 30 pA). (d) Schematic model of the Co-atom adsorption on the 2D-MOF/Cu(111) and STM topographic image of Co atom adsorbed on the Ph_4DN MOF/Cu (111) (24 × 19 nm^2, 30 pA, 750 mV). Three types of nanopores are observed: (I) empty pores, (II) filled pores, and (III) pores with motifs. (e) Left panels: STM topographic image (11 × 11 nm^2, V_s = −2.0 V, I_t = 30 pA) and the simultaneously obtained dI/dV map at −0.60 V. Right panel: 3D dI/dV plot along the boxed region in the 2D map (left), showing an increased LDOS in the Co adsorption area between −0.7 and −1.5 eV, distinct from the LDOS of Ph_4DN. (f) STM topographic image after Co atom deposition on the nanopore array (14 × 11 nm^2, V_s = −750 mV, I_t = 30 pA). Arrows indicate adsorbed Co atoms. The lower panel denotes calculated structures representing possible configurations of Co–Ph_4DN complexes within a nanopore.

MOF is stronger than that between the adsorbed Co atoms and the 2D MOF, allowing the original 2D MOF structure to remain intact after Co adsorption. Although the results may appear straightforward at first glance, the presence of Co dots inside the 2D MOF nanopores, as shown in the lower panel of Fig. 3d, carries an important implication: Co atoms do not disrupt the 2D MOF structure. This behavior contrasts sharply with Co adsorption on 2D MOFs supported on Ag(111).[64] Instead, the Co deposition yields three distinct types of nanopores: (I) empty, (II) trapped Ph_4DN, and (III) Co–Ph_4DN coordinated motifs, as illustrated in the lower panel of Fig. 3d.

Another critical aspect is whether the adsorbed Co atoms interact with the 2D MOF *via* chemisorption. If a chemical bond forms between the Co atom and the Ph_4DN molecule, the LDOS would change. To assess this, we compared the electronic structure of the MOF at locations with and without Co atom adsorption to determine whether it remains unchanged.

Fig. 3e presents an STM topographic image (upper left panel) and the corresponding dI/dV map acquired at −0.6 V (lower left panel), following the deposition of Co atoms at a density of approximately one atom per 2.4 × 2.4 nm^2. In the dI/dV map, the red-to-blue color scale represents the LDOS intensity, with blue indicating higher LDOS. The Ph_4DN molecules forming the honeycomb lattice appear as regions of suppressed LDOS, while the interiors of the nanopores are relatively brighter.

Notably, these results show that the original Cu–Ph_4DN coordination framework remained intact following Co deposition. This stability underscores the robustness of the Cu–Ph_4DN bonding.

It is important to note that while the topographic images cannot distinguish whether the bright spots within the nanopores correspond to Co atoms or Ph_4DN molecules, STS–LDOS measurements can. This is because the Co clusters exhibit

LDOS signatures that are clearly distinct from those of the Ph_4DN molecules. The right panel of Fig. 3e displays a 3D dI/dV map, where the x-, y-, and z-axes represent the lateral position (in nm), energy relative to the Fermi level ($E - E_F$, in eV), and dI/dV intensity (in nA/V), respectively. This data was acquired from the region marked by the box in the dI/dV map at −0.6 V (lower-left panel of Fig. 3e), which includes both a Co atom and surrounding Ph_4DN molecules. The map reveals a broad LDOS distribution associated with the Co clusters, spanning an energy range from approximately −0.8 to −1.5 eV. The bottom panel of Fig. 3e presents the dI/dV spectra acquired on Cu(111) (black), the Ph_4DN MOF (red), and the Co dots (blue). The Co dots exhibit a markedly enhanced LDOS, significantly greater than that of the Ph_4DN MOF. These STS measurements in Fig. 3e clearly demonstrate that the electronic structure of the original Ph_4DN framework remains intact after Co atom deposition. This indicates that the Co atoms are unlikely to form covalent bonds with the Ph_4DN molecules.

Interestingly, we observed an increase in bright dots within the 2D MOF nanopores following Co deposition (Fig. 3d and e), along with other distinctive patterns that frequently appeared within the pores. Fig. 3f shows an STM topographic image revealing three characteristic configurations within the nanopores: (I) empty pores, (II) pores containing trapped Ph_4DN molecules, which can diffuse continuously as observed on bare Cu(111) (Fig. 2b), and (III) pores exhibiting sixfold symmetry consistent with the hexagonal geometry of the pore. The relative distribution of these configurations was quantified as: I – 73.5%, II – 17.4%, and III – 9.1%. It is known that linear nitrile-terminated molecules can coordinate with Co centers to form sixfold symmetric motifs on metal substrates at 78 K.[65] Accordingly, the observed sixfold symmetry likely arises from an ensemble effect, resulting from the rapid rotation of the C_3 coordination complex within the nanopore, combined with the slower scanning speed of the STM tip.

However, since configuration III was not observed prior to Co atom adsorption, a plausible formation mechanism involves a single Co atom becoming trapped by diffusing Ph_4DN molecules, leading to the formation of a Co–Ph_4DN coordination complex within the nanopore as we expected in Fig. 1a, namely, if a Co atom encounters other Co atoms within the same nanopore, it immediately forms a Co nanocluster; however, if it encounters a Ph_4DN molecule, it can form a stable Co–Ph_4DN coordination motif within the nanopore.

From a computational perspective, both Cu and Co belong to the 3d transition metal series and are expected to exhibit similar coordination behavior. Therefore, achieving a C_6 symmetric coordination between a Co atom and Ph_4DN molecules within the nanopore is unlikely, in contrast to the well-known C_6 coordination formed by six terphenyl-4,4″-dicarbonitrile molecules around a Co center on Ag(111).[64] This is because Cu adatoms are known to form only C_2 and C_3 symmetric coordination geometries (see SI, Fig. S8), and the same limitation is expected to apply to Co atoms.

To gain more insights the energetically favorable configurations of three Ph_4DN molecules confined within a nanopore in the absence of a Co atom, we performed MLIP calculations (the lower panel in Fig. 3f and SI, Fig. S16). In this case, the three Ph_4DN molecules adopt chiral arrangements, similar to those observed in the 2D MOF formed on Ag(111) using the linear ditopic *para*-sexiphenyl-dicarbonitrile (NC-Ph6-CN).[65] This chiral configuration lies completely flat on the substrate surface and provides sufficient space for continuous rotational motion.

However, our calculations for three Ph_4DN molecules within a 2D MOF nanopore on Cu(111) in the presence of a Co atom (Fig. 3f) indicate that the C_3-symmetric coordination of the Ph_4DN molecules around the central Co atom shown in Fig. 3f is significantly more stable (ΔE = 0.00 eV) than the chiral configuration (ΔE = +2.25 eV, SI, Fig. S16c). This C_3 coordination, anchored by the central Co atom, may exhibit rotational dynamics and produce a six-fold symmetric STM image.

However, the experimentally observed the configuration III in the STM image in Fig. 3f is clearly distinct from that of the rotating C_3 configuration without Co atoms.[65] Specifically, the center of the pore appears darker rather than brighter, suggesting that the Co adatom may reside between the Cu substrate and the molecules, akin to the behavior of Cu adatoms. Furthermore, no chirality is observed in the STM image in Fig. 3d, indicating that the Co-induced coordination motif is not chiral. These observations support the conclusion that Co atom adsorption induces a C_3 coordination motif, where the Ph_4DN molecules are pinned by the central Co atom. Although it remains uncertain whether the coordinated Ph_4DN molecules exhibit rotational motion, it is evident that they do not adopt the chiral coordination proposed for NC–Ph_6–CN on Ag(111) in the absence of a Co atom.[65]

Finally, additional important observation in Fig. 3f is the presence of two nanopores exhibiting configuration III. While the nanopore on the right side maintains a hexagonal shape, the one on the left shows a distorted hexagonal geometry. Despite this difference in shape, both display the same symmetric features within the nanopores. This suggests that even when nanopores are deformed, it is still possible to fabricate Co-atom coordination with the same symmetry inside them.

4. Conclusions

In conclusion, our combined experimental results from STM/STS and ARPES, together with theoretical MLIP/DFT calculations, demonstrate that Co-atom spin coordination with S ~ 1/2 can be achieved using a robust 2 nm-sized nanopore array in a 2D MOF on Cu(111). Ph_4DN precursor molecules can be deposited directly on the Cu(111) surface at 300 K or higher, or alternatively *via* post-deposition annealing, preferentially forming honeycomb networks that fully cover the surface, as C_3 coordination around Cu adatoms is energetically favorable.

Importantly, this 2D MOF on Cu(111) is formed without the deposition of additional 3d-transition-metal atoms (*e.g.*, Fe, Co, or Ni), resulting in a nonmagnetic Cu-adatom–coordinated

framework. This nonmagnetic character is crucial for spin-related studies or applications, as magnetic exchange coupling or stray fields from a magnetic MOF could interfere with the intrinsic spins of guest 3d atoms within the nanopores.

Once the honeycomb nanopores are established, additional Ph_4DN molecules can be trapped within the pores and diffuse thermally. Subsequent deposition of Co atoms into the nanopores allows the formation of Co–Ph_4DN coordination motifs. Furthermore, the 2D MOF nanopore array constructed from Cu adatoms offers significant versatility. The 2 nm-sized nanopores can host guest transition-metal atoms and organic molecules, providing a promising platform for single-atom electronics, spintronic devices, quantum materials, and catalytic applications.

Author contributions

T. K. Y. conceived and designed the project. H. I., R. I., and T. K. Y. performed all STM and STS experiments. K. T., R. H., and Y. K. conducted machine learning and DFT calculations. M. C., T. K., C. C., and M. H. synthesized the organic molecules. H. I., R. S., F. N., K. F., and S. K. carried out ARPES measurements. H. I. and T. K. Y. wrote the initial draft, and T. K. Y. refined and finalized the manuscript. All authors discussed the results and provided comments on the manuscript.

Conflicts of interest

There are no conflicts to declare.

Data availability

The data supporting this study are available from the corresponding author upon reasonable request.

Supplementary information (SI) is available. See DOI: https://doi.org/10.1039/d6nr00051g.

Acknowledgements

This work was supported by JSPS KAKENHI Grant Number 23H02033 and 25K08589, the Murata Science Foundation, the Shorai Foundation for Science and Technology, the TEPCO Memorial Foundation, the Casio Science Promotion Foundation, and the Toshiaki Ogasawara Memorial Foundation.

References

1 H. V. Babu, M. G. M. Bai and M. Rajeswara Rao, Functional π-Conjugated Two-Dimensional Covalent Organic Frameworks, *ACS Appl. Mater. Interfaces*, 2019, **11**(12), 11029–11060, DOI: 10.1021/acsami.8b19087.

2 D. Bessinger, L. Ascherl, F. Auras and T. Bein, Spectrally Switchable Photodetection with Near-Infrared-Absorbing Covalent Organic Frameworks, *J. Am. Chem. Soc.*, 2017, **139**(34), 12035–12042, DOI: 10.1021/jacs.7b06599.

3 M. O. Blunt, J. C. Russell, N. R. Champness and P. H. Beton, Templating Molecular Adsorption Using a Covalent Organic Framework, *Chem. Commun.*, 2010, **46**(38), 7157, DOI: 10.1039/c0cc01810d.

4 H. Chen, H. Tu, C. Hu, Y. Liu, D. Dong, Y. Sun, Y. Dai, S. Wang, H. Qian, Z. Lin and L. Chen, Cationic Covalent Organic Framework Nanosheets for Fast Li-Ion Conduction, *J. Am. Chem. Soc.*, 2018, **140**(3), 896–899, DOI: 10.1021/jacs.7b12292.

5 D. Cui, D. F. Perepichka, J. M. MacLeod and F. Rosei, Surface-Confined Single-Layer Covalent Organic Frameworks: Design, Synthesis and Application, *Chem. Soc. Rev.*, 2020, **49**(7), 2020–2038, DOI: 10.1039/C9CS00456D.

6 G. Das, B. P. Biswal, S. Kandambeth, V. Venkatesh, G. Kaur, M. Addicoat, T. Heine, S. Verma and R. Banerjee, Chemical Sensing in Two Dimensional Porous Covalent Organic Nanosheets, *Chem. Sci.*, 2015, **6**(7), 3931–3939, DOI: 10.1039/C5SC00512D.

7 J. F. Dienstmaier, D. D. Medina, M. Dogru, P. Knochel, T. Bein, W. M. Heckl and M. Lackinger, Isoreticular Two-Dimensional Covalent Organic Frameworks Synthesized by On-Surface Condensation of Diboronic Acids, *ACS Nano*, 2012, **6**(8), 7234–7242, DOI: 10.1021/nn302363d.

8 C. M. Doyle, C. McGuinness, A. P. Lawless, A. B. Preobrajenski, N. A. Vinogradov and A. A. Cafolla, Surface Mediated Synthesis of 2D Covalent Organic Networks: 1,3,5−Tris(4−bromophenyl)Benzene on Au(111), *Phys. Status Solidi B*, 2019, **256**(2), 1800349, DOI: 10.1002/pssb.201800349.

9 X. Feng, X. Ding and D. Jiang, Covalent Organic Frameworks, *Chem. Soc. Rev.*, 2012, **41**(18), 6010, DOI: 10.1039/c2cs35157a.

10 H. Furukawa and O. M. Yaghi, Storage of Hydrogen, Methane, and Carbon Dioxide in Highly Porous Covalent Organic Frameworks for Clean Energy Applications, *J. Am. Chem. Soc.*, 2009, **131**(25), 8875–8883, DOI: 10.1021/ja9015765.

11 Q. Gao, X. Li, G.-H. Ning, K. Leng, B. Tian, C. Liu, W. Tang, H.-S. Xu and K. P. Loh, Highly Photoluminescent Two-Dimensional Imine-Based Covalent Organic Frameworks for Chemical Sensing, *Chem. Commun.*, 2018, **54**(19), 2349–2352, DOI: 10.1039/C7CC09866A.

12 L. Ge, C. Qiao, Y. Tang, X. Zhang and X. Jiang, Light-Activated Hypoxia-Sensitive Covalent Organic Framework for Tandem-Responsive Drug Delivery, *Nano Lett.*, 2021, **21**(7), 3218–3224, DOI: 10.1021/acs.nanolett.1c00488.

13 R. Gutzler, H. Walch, G. Eder, S. Kloft, W. M. Heckl and M. Lackinger, Surface Mediated Synthesis of 2D Covalent Organic Frameworks: 1,3,5-Tris(4-Bromophenyl)Benzene on Graphite(001), Cu(111), and Ag(110), *Chem. Commun.*, 2009, **29**, 4456, DOI: 10.1039/b906836h.

14 Z. Hao, L. Song, C. Yan, H. Zhang, Z. Ruan, S. Sun, J. Lu and J. Cai, On-Surface Synthesis of One-Type Pore Single-Crystal

Porous Covalent Organic Frameworks, *Chem. Commun.*, 2019, **55**(72), 10800–10803, DOI: 10.1039/C9CC04561A.

15 N. Huang, X. Chen, R. Krishna and D. Jiang, Two-Dimensional Covalent Organic Frameworks for Carbon Dioxide Capture through Channel-Wall Functionalization, *Angew. Chem., Int. Ed.*, 2015, **54**(10), 2986–2990, DOI: 10.1002/anie.201411262.

16 T. K. Yamada, S. Kanazawa, K. Fukutani and S. Kera, Growth of Transition-Metal Cobalt Nanoclusters on 2D Covalent Organic Frameworks, *J. Phys. Chem. C*, 2024, **128**(3), 1477–1486, DOI: 10.1021/acs.jpcc.3c07435.

17 A. P. Cote, A. I. Benin, N. W. Ockwig, M. O'Keeffe, A. J. Matzger and O. M. Yaghi, Porous, Crystalline, Covalent Organic Frameworks, *Science*, 2005, **310**, 1166–1170, DOI: 10.1126/science.1120411.

18 C. Barreteau, F. Ducastelle and T. Mallah, A Bird's Eye View on the Flat and Conic Band World of the Honeycomb and Kagome Lattices: Towards an Understanding of 2D Metal-Organic Frameworks Electronic Structure, *J. Phys.: Condens. Matter*, 2017, **29**(46), 465302, DOI: 10.1088/1361-648X/aa8fec.

19 B. Chen, M. Eddaoudi, S. T. Hyde, M. O'Keeffe and O. M. Yaghi, Interwoven Metal-Organic Framework on a Periodic Minimal Surface with Extra-Large Pores, *Science*, 2001, **291**(5506), 1021–1023, DOI: 10.1126/science.1056598.

20 B. De La Torre, M. Švec, P. Hapala, J. Redondo, O. Krejčí, R. Lo, D. Manna, A. Sarmah, D. Nachtigallová, J. Tuček, P. Błoński, M. Otyepka, R. Zbořil, P. Hobza and P. Jelínek, Non-Covalent Control of Spin-State in Metal-Organic Complex by Positioning on N-Doped Graphene, *Nat. Commun.*, 2018, **9**(1), 2831, DOI: 10.1038/s41467-018-05163-y.

21 R. S. Forgan, The Surface Chemistry of Metal–Organic Frameworks and Their Applications, *Dalton Trans.*, 2019, **48**(25), 9037–9042, DOI: 10.1039/C9DT01710K.

22 H. Furukawa, N. Ko, Y. B. Go, N. Aratani, S. B. Choi, E. Choi, A.Ö Yazaydin, R. Q. Snurr, M. O'Keeffe, J. Kim and O. M. Yaghi, Ultrahigh Porosity in Metal-Organic Frameworks, *Science*, 2010, **329**(5990), 424–428, DOI: 10.1126/science.1192160.

23 X. Ge, H. Di, P. Wang, X. Miao, P. Zhang, H. Wang, J. Ma and L. Yin, Metal–Organic Framework-Derived Nitrogen-Doped Cobalt Nanocluster Inlaid Porous Carbon as High-Efficiency Catalyst for Advanced Potassium–Sulfur Batteries, *ACS Nano*, 2020, **14**(11), 16022–16035, DOI: 10.1021/acsnano.0c07658.

24 W.-T. Koo, J.-S. Jang and I.-D. Kim, Metal-Organic Frameworks for Chemiresistive Sensors, *Chem*, 2019, **5**(8), 1938–1963, DOI: 10.1016/j.chempr.2019.04.013.

25 C. Krull, M. Castelli, P. Hapala, D. Kumar, A. Tadich, M. Capsoni, M. T. Edmonds, J. Hellerstedt, S. A. Burke, P. Jelinek and A. Schiffrin, Iron-Based Trinuclear Metal-Organic Nanostructures on a Surface with Local Charge Accumulation, *Nat. Commun.*, 2018, **9**(1), 3211, DOI: 10.1038/s41467-018-05543-4.

26 A. Kumar, K. Banerjee, A. S. Foster and P. Liljeroth, Two-Dimensional Band Structure in Honeycomb Metal–Organic Frameworks, *Nano Lett.*, 2018, **18**(9), 5596–5602, DOI: 10.1021/acs.nanolett.8b02062.

27 R. Makiura, S. Motoyama, Y. Umemura, H. Yamanaka, O. Sakata and H. Kitagawa, Surface Nano-Architecture of a Metal–Organic Framework, *Nat. Mater.*, 2010, **9**(7), 565–571, DOI: 10.1038/nmat2769.

28 C. V. McGuire and R. S. Forgan, The Surface Chemistry of Metal–Organic Frameworks, *Chem. Commun.*, 2015, **51**(25), 5199–5217, DOI: 10.1039/C4CC04458D.

29 Y. Peng, Y. Li, Y. Ban and W. Yang, Two–Dimensional Metal–Organic Framework Nanosheets for Membrane–Based Gas Separation, *Angew. Chem.*, 2017, **129**(33), 9889–9893, DOI: 10.1002/ange.201703959.

30 H. Sun, S. Tan, M. Feng, J. Zhao and H. Petek, Deconstruction of the Electronic Properties of a Topological Insulator with a Two-Dimensional Noble Metal–Organic Honeycomb–Kagome Band Structure, *J. Phys. Chem. C*, 2018, **122**(32), 18659–18668, DOI: 10.1021/acs.jpcc.8b03353.

31 E. Virmani, J. M. Rotter, A. Mähringer, T. von Zons, A. Godt, T. Bein, S. Wuttke and D. D. Medina, On-Surface Synthesis of Highly Oriented Thin Metal–Organic Framework Films through Vapor-Assisted Conversion, *J. Am. Chem. Soc.*, 2018, **140**(14), 4812–4819, DOI: 10.1021/jacs.7b08174.

32 A. Yamauchi, K. Tanaka, M. Fuki, S. Fujiwara, N. Kimizuka, T. Ryu, M. Saigo, K. Onda, R. Kusumoto, N. Ueno, H. Sato, Y. Kobori, K. Miyata and N. Yanai, Room-temperature quantum coherence of entangled multiexcitons in a metal-organic framework, *Sci. Adv.*, 2024, **10**(1), eadi3147, DOI: 10.1126/sciadv.adi3147.

33 Z. Liu, W. He and Z. Guo, Metal Coordination in Photoluminescent Sensing, *Chem. Soc. Rev.*, 2013, **42**(4), 1568, DOI: 10.1039/c2cs35363f.

34 G. E. Kostakis, A. M. Ako and A. K. Powell, Structural Motifs and Topological Representation of Mn Coordination Clusters, *Chem. Soc. Rev.*, 2010, **39**(6), 2238, DOI: 10.1039/b918192j.

35 P. J. Stang and B. Olenyuk, Self-Assembly, Symmetry, and Molecular Architecture: Coordination as the Motif in the Rational Design of Supramolecular Metallacyclic Polygons and Polyhedra, *Acc. Chem. Res.*, 1997, **30**(12), 502–518, DOI: 10.1021/ar9602011.

36 G. F. Swiegers and T. J. Malefetse, New Self-Assembled Structural Motifs in Coordination Chemistry, *Chem. Rev.*, 2000, **100**(9), 3483–3538, DOI: 10.1021/cr990110s.

37 E. Khare, N. Holten-Andersen and M. J. Buehler, Transition-Metal Coordinate Bonds for Bioinspired Macromolecules with Tunable Mechanical Properties, *Nat. Rev. Mater.*, 2021, **6**(5), 421–436, DOI: 10.1038/s41578-020-00270-z.

38 A. M. Ako, V. Mereacre, I. J. Hewitt, R. Clérac, L. Lecren, C. E. Anson and A. K. Powell, Enhancing Single Molecule Magnet Parameters. Synthesis, Crystal Structures and Magnetic Properties of Mixed-Valent Mn $_4$ SMMs, *J. Mater. Chem.*, 2006, **16**(26), 2579–2586, DOI: 10.1039/B604611H.

39 A. Bagrets, S. Schmaus, A. Jaafar, D. Kramczynski, T. K. Yamada, M. Alouani, W. Wulfhekel and F. Evers, Single Molecule Magnetoresistance with Combined Antiferromagnetic and Ferromagnetic Electrodes, *Nano Lett.*, 2012, **12**(10), 5131–5136, DOI: 10.1021/nl301967t.

40 S. Bertaina, S. Gambarelli, T. Mitra, B. Tsukerblat, A. Müller and B. Barbara, Quantum Oscillations in a Molecular Magnet, *Nature*, 2008, **453**(7192), 203–206, DOI: 10.1038/nature06962.

41 J. Brand, S. Gozdzik, N. Néel, J. L. Lado, J. Fernández-Rossier and J. Kröger, Electron and Cooper-Pair Transport across a Single Magnetic Molecule Explored with a Scanning Tunneling Microscope, *Phys. Rev. B*, 2018, **97**(19), 195429, DOI: 10.1103/PhysRevB.97.195429.

42 X. Chen, Y.-S. Fu, S.-H. Ji, T. Zhang, P. Cheng, X.-C. Ma, X.-L. Zou, W.-H. Duan, J.-F. Jia and Q.-K. Xue, Probing Superexchange Interaction in Molecular Magnets by Spin-Flip Spectroscopy and Microscopy, *Phys. Rev. Lett.*, 2008, **101**(19), 197208, DOI: 10.1103/PhysRevLett.101.197208.

43 A. Cini, M. Mannini, F. Totti, M. Fittipaldi, G. Spina, A. Chumakov, R. Rüffer, A. Cornia and R. Sessoli, Mössbauer Spectroscopy of a Monolayer of Single Molecule Magnets, *Nat. Commun.*, 2018, **9**(1), 480, DOI: 10.1038/s41467-018-02840-w.

44 T. Frauhammer, H. Chen, T. Balashov, G. Derenbach, S. Klyatskaya, E. Moreno-Pineda, M. Ruben and W. Wulfhekel, Indirect Spin-Readout of Rare-Earth-Based Single-Molecule Magnet with Scanning Tunneling Microscopy, *Phys. Rev. Lett.*, 2021, **127**(12), 123201, DOI: 10.1103/PhysRevLett.127.123201.

45 M. T. Gamer, Y. Lan, P. W. Roesky, A. K. Powell and R. Clérac, Pentanuclear Dysprosium Hydroxy Cluster Showing Single-Molecule-Magnet Behavior, *Inorg. Chem.*, 2008, **47**(15), 6581–6583, DOI: 10.1021/ic8008255.

46 M. Ganzhorn, S. Klyatskaya, M. Ruben and W. Wernsdorfer, Strong Spin–Phonon Coupling between a Single-Molecule Magnet and a Carbon Nanotube Nanoelectromechanical System, *Nat. Nanotechnol.*, 2013, **8**(3), 165–169, DOI: 10.1038/nnano.2012.258.

47 J. E. Grose, E. S. Tam, C. Timm, M. Scheloske, B. Ulgut, J. J. Parks, H. D. Abruña, W. Harneit and D. C. Ralph, Tunnelling Spectra of Individual Magnetic Endofullerene Molecules, *Nat. Mater.*, 2008, **7**(11), 884–889, DOI: 10.1038/nmat2300.

48 C. F. Hirjibehedin, C.-Y. Lin, A. F. Otte, M. Ternes, C. P. Lutz, B. A. Jones and A. J. Heinrich, Large Magnetic Anisotropy of a Single Atomic Spin Embedded in a Surface Molecular Network, *Science*, 2007, **317**(5842), 1199–1203, DOI: 10.1126/science.1146110.

49 J. Homberg, A. Weismann, R. Berndt and M. Gruber, Inducing and Controlling Molecular Magnetism through Supramolecular Manipulation, *ACS Nano*, 2020, **14**(12), 17387–17395, DOI: 10.1021/acsnano.0c07574.

50 R. Kawaguchi, K. Hashimoto, T. Kakudate, K. Katoh, M. Yamashita and T. Komeda, Spatially Resolving Electron Spin Resonance of π-Radical in Single-Molecule Magnet, *Nano Lett.*, 2023, **23**(1), 213–219, DOI: 10.1021/acs.nanolett.2c04049.

51 S. L. Kawahara, J. Lagoute, V. Repain, C. Chacon, Y. Girard, S. Rousset, A. Smogunov and C. Barreteau, Large Magnetoresistance through a Single Molecule Due to a Spin-Split Hybridized Orbital, *Nano Lett.*, 2012, **12**(9), 4558–4563, DOI: 10.1021/nl301802e.

52 L. Liu, K. Yang, Y. Jiang, B. Song, W. Xiao, S. Song, S. Du, M. Ouyang, W. A. Hofer, A. H. Castro Neto and H.-J. Gao, Revealing the Atomic Site-Dependent g Factor within a Single Magnetic Molecule via the Extended Kondo Effect, *Phys. Rev. Lett.*, 2015, **114**(12), 126601, DOI: 10.1103/PhysRevLett.114.126601.

53 W. Wulfhekel, T. Miyamachi, S. Schmaus, T. K. Yamada, A. F. Takacs, A. Bagrets, F. Evers, T. Balashov, M. Gruber, V. Davesne, M. Bowen and E. Beaurepaire, Spintronics with Single Molecules, in *2012 12th IEEE International Conference on Nanotechnology (IEEE-NANO)*, IEEE, Birmingham, United Kingdom, 2012, pp. 1–5. DOI: 10.1109/NANO.2012.6322103.

54 A. Bagrets, S. Schmaus, A. Jaafar, D. Kramczynski, T. K. Yamada, M. Alouani, W. Wulfhekel and F. Evers, Single Molecule Magnetoresistance with Combined Antiferromagnetic and Ferromagnetic Electrodes, *Nano Lett.*, 2012, **12**(10), 5131–5136, DOI: 10.1021/nl301967t.

55 L. Gerhard, T. K. Yamada, T. Balashov, A. F. Takács, R. J. H. Wesselink, M. Däne, M. Fechner, S. Ostanin, A. Ernst, I. Mertig and W. Wulfhekel, Magnetoelectric Coupling at Metal Surfaces, *Nat. Nanotechnol.*, 2010, **5**(11), 792–797, DOI: 10.1038/nnano.2010.214.

56 X. Xie, C. He, B. Li, Y. He, D. A. Cullen, E. C. Wegener, A. J. Kropf, U. Martinez, Y. Cheng, M. H. Engelhard, M. E. Bowden, M. Song, T. Lemmon, X. S. Li, Z. Nie, J. Liu, D. J. Myers, P. Zelenay, G. Wang, G. Wu, V. Ramani and Y. Shao, Performance Enhancement and Degradation Mechanism Identification of a Single-Atom Co–N–C Catalyst for Proton Exchange Membrane Fuel Cells, *Nat. Catal.*, 2020, **3**(12), 1044–1054, DOI: 10.1038/s41929-020-00546-1.

57 D. Zhou, X. Li, H. Shang, F. Qin and W. Chen, Atomic Regulation of Metal–Organic Framework Derived Carbon-Based Single-Atom Catalysts for the Electrochemical CO_2 Reduction Reaction, *J. Mater. Chem. A*, 2021, **9**(41), 23382–23418, DOI: 10.1039/D1TA06915B.

58 Single Atom Catalysts Push the Boundaries of Heterogeneous Catalysis, *Nat. Commun.*, 2021, **12**(1), DOI: 10.1038/s41467-021-26130-0.

59 S. Zint, D. Ebeling, T. Schlöder, S. Ahles, D. Mollenhauer, H. A. Wegner and A. Schirmeisen, Imaging Successive Intermediate States of the On-Surface Ullmann Reaction on Cu(111): Role of the Metal Coordination, *ACS Nano*, 2017, **11**(4), 4183–4190, DOI: 10.1021/acsnano.7b01109.

60 T. K. Yamada, R. Nemoto, H. Ishii, F. Nishino, Y.-H. Chang, C.-H. Wang, P. Krüger and M. Horie, Designing 2D Stripe Winding Network through Crown-Ether Intermediate Ullmann Coupling on Cu(111) Surface, *Nanoscale Horiz.*, 2024, **9**(5), 718–730, DOI: 10.1039/D3NH00586K.

61 W. Wang, X. Shi, S. Wang, M. A. Van Hove and N. Lin, Single-Molecule Resolution of an Organometallic Intermediate in a Surface-Supported Ullmann Coupling Reaction, *J. Am. Chem. Soc.*, 2011, **133**(34), 13264–13267, DOI: 10.1021/ja204956b.

62 L. Song, B. Yang, F. Liu, K. Niu, Y. Han, J. Wang, Y. Zheng, H. Zhang, Q. Li and L. Chi, Synthesis of Two-Dimensional Metal–Organic Frameworks via Dehydrogenation Reactions on a Cu(111) Surface, *J. Phys. Chem. C*, 2020, **124**(23), 12390–12396, DOI: 10.1021/acs.jpcc.0c00931.

63 S. Stepanow, N. Lin, D. Payer, U. Schlickum, F. Klappenberger, G. Zoppellaro, M. Ruben, H. Brune, J. V. Barth and K. Kern, Surface–Assisted Assembly of 2D Metal–Organic Networks That Exhibit Unusual Threefold Coordination Symmetry, *Angew. Chem.*, 2007, **119**(5), 724–727, DOI: 10.1002/ange.200603644.

64 U. Schlickum, F. Klappenberger, R. Decker, G. Zoppellaro, S. Klyatskaya, M. Ruben, K. Kern, H. Brune and J. V. Barth, Surface-Confined Metal–Organic Nanostructures from Co-Directed Assembly of Linear Terphenyl-Dicarbonitrile Linkers on Ag(111), *J. Phys. Chem. C*, 2010, **114**(37), 15602–15606, DOI: 10.1021/jp104518h.

65 D. Kühne, F. Klappenberger, W. Krenner, S. Klyatskaya, M. Ruben and J. V. Barth, Rotational and Constitutional Dynamics of Caged Supramolecules, *Proc. Natl. Acad. Sci. U. S. A.*, 2010, **107**(50), 21332–21336, DOI: 10.1073/pnas.1008991107.

66 J. Li, I. Piquero-Zulaica, S. Gottardi, M. A. Ashoush, Z. M. Abd El-Fattah, L. Solianyk, J. E. Ortega, J. V. Barth, J. C. Moreno-Lopez, J. Lobo-Checa and M. Stöhr, An Organic Array of Quantum Corrals Modulated by the Gold Herringbone Electronic Superlattice, *Nanoscale*, 2025, **17**(16), 10314–10323, DOI: 10.1039/D5NR00148J.

67 M. Pivetta, G. E. Pacchioni, U. Schlickum, J. V. Barth and H. Brune, Formation of Fe Cluster Superlattice in a Metal-Organic Quantum-Box Network, *Phys. Rev. Lett.*, 2013, **110**(8), 086102, DOI: 10.1103/PhysRevLett.110.086102.

68 I. Piquero-Zulaica, J. Lobo-Checa, Z. M. A. El-Fattah, J. E. Ortega, F. Klappenberger, W. Auwärter and J. V. Barth, Engineering Quantum States and Electronic Landscapes through Surface Molecular Nanoarchitectures, *Rev. Mod. Phys.*, 2022, **94**(4), 045008, DOI: 10.1103/RevModPhys.94.045008.

69 J. Lobo-Checa, L. Hernández-López, M. M. Otrokov, I. Piquero-Zulaica, A. E. Candia, P. Gargiani, D. Serrate, F. Delgado, M. Valvidares, J. Cerdá, A. Arnau and F. Bartolomé, Ferromagnetism on an Atom-Thick & Extended 2D Metal-Organic Coordination Network, *Nat. Commun.*, 2024, **15**(1), 1858, DOI: 10.1038/s41467-024-46115-z.

70 E. Isufi Neziri, C. Hensky, H. Q. Le, D. Radillo Ochoa, A. Cebrat, M. Parschau, K. Ernst and C. Wäckerlin, 2D Metalorganic Ferromagnets, *Adv. Sci.*, 2025, **12**(16), 2415266, DOI: 10.1002/advs.202415266.

71 N. K. M. Nazriq, P. Krüger and T. K. Yamada, Carbon Monoxide Stripe Motion Driven by Correlated Lateral Hopping in a 1.4 × 1.4 Monolayer Phase on Cu(111), *J. Phys. Chem. Lett.*, 2020, **11**(5), 1753–1761, DOI: 10.1021/acs.jpclett.9b03645.

72 R. Nemoto, P. Krüger, A. N. Putri Hartini, T. Hosokai, M. Horie, S. Kera and T. K. Yamada, Well-Ordered Monolayer Growth of Crown-Ether Ring Molecules on Cu (111) in Ultra-High Vacuum: An STM, UPS, and DFT Study, *J. Phys. Chem. C*, 2019, **123**(31), 18939–18950, DOI: 10.1021/acs.jpcc.9b03335.

73 E. Inami, M. Yamaguchi, T. Yamaguchi, M. Shimasaki and T. K. Yamada, Controlled Deposition Number of Organic Molecules Using Quartz Crystal Microbalance Evaluated by Scanning Tunneling Microscopy Single-Molecule-Counting, *Anal. Chem.*, 2018, **90**(15), 8954–8959, DOI: 10.1021/acs.analchem.8b01118.

74 I. Horcas, R. Fernández, J. M. Gómez-Rodríguez, J. Colchero, J. Gómez-Herrero and A. M. Baro, WSXM: A Software for Scanning Probe Microscopy and a Tool for Nanotechnology, *Rev. Sci. Instrum.*, 2007, **78**(1), 013705, DOI: 10.1063/1.2432410.

75 Y. Yamagishi, S. Nakashima, K. Oiso and T. K. Yamada, Recovery of Nanomolecular Electronic States from Tunneling Spectroscopy: LDOS of Low-Dimensional Phthalocyanine Molecular Structures on Cu(111), *Nanotechnology*, 2013, **24**(39), 395704, DOI: 10.1088/0957-4484/24/39/395704.

76 E. Inami, P. Krüger, H. Hayashi and T. K. Yamada, Emergence of Robust 1D Atomic and Electronic Textures in Mn Ultrathin Films via Antiferromagnet–Ferromagnet Interfaces, *Small*, 2025, e04791, DOI: 10.1002/smll.202504791.

77 T. K. Yamada, T. Abe, N. M. K. Nazriq and T. Irisawa, Electron-Bombarded ⟨110⟩-Oriented Tungsten Tips for Stable Tunneling Electron Emission, *Rev. Sci. Instrum.*, 2016, **87**(3), 033703, DOI: 10.1063/1.4943074.

78 T. Yamaguchi, E. Inami, Y. Goto, Y. Sakai, S. Sasaki, T. Ohno and T. K. Yamada, Fabrication of Tungsten Tip Probes within 3 s by Using Flame Etching, *Rev. Sci. Instrum.*, 2019, **90**(6), 063701, DOI: 10.1063/1.5085251.

79 Y. Goto, R. Suizu, Y. Noguchi and T. K. Yamada, Oxidative Vaporization Etching for Molybdenum Tip Formation in Air, *Appl. Surf. Sci.*, 2021, **542**, 148642, DOI: 10.1016/j.apsusc.2020.148642.

80 T. K. Yamada, N. K. M. Nazriq and K. Tada, Stabilization of Isolated Fe Atoms on a 1-Nm-Thick MgO/Fe(001) Insulating Surface via Critical Tunneling for a Robust Quantum Spin Platform, *Appl. Surf. Sci. Adv.*, 2026, **33**, 100965, DOI: 10.1016/j.apsadv.2026.100965.

81 T. K. Yamada, R. Nemoto, F. Nishino, T. Hosokai, C.-H. Wang, M. Horie, Y. Hasegawa, S. Kera and P. Krüger, On-Surface Growth of Transition-Metal Cobalt Nanoclusters Using a 2D Crown-Ether Array, *J. Mater. Chem. C*, 2024, **12**, 874, DOI: 10.1039/D3TC03339B.

82 K. Wan, J. He and X. Shi, Construction of High Accuracy Machine Learning Interatomic Potential for Surface/Interface of Nanomaterials—A Review, *Adv. Mater.*, 2024, **36**(22), 2305758, DOI: 10.1002/adma.202305758.

83 S. Takamoto, C. Shinagawa, D. Motoki, K. Nakago, W. Li, I. Kurata, T. Watanabe, Y. Yayama, H. Iriguchi, Y. Asano, T. Onodera, T. Ishii, T. Kudo, H. Ono, R. Sawada, R. Ishitani, M. Ong, T. Yamaguchi, T. Kataoka, A. Hayashi, N. Charoenphakdee and T. Ibuka, Towards Universal Neural Network Potential for Material Discovery Applicable to Arbitrary Combination of 45 Elements, *Nat. Commun.*, 2022, **13**(1), 2991, DOI: 10.1038/s41467-022-30687-9.

84 H. Takagi, T. Takayama, G. Jackeli, G. Khaliullin and S. E. Nagler, Concept and Realization of Kitaev Quantum Spin Liquids, *Nat. Rev. Phys.*, 2019, **1**(4), 264–280, DOI: 10.1038/s42254-019-0038-2.

85 T. K. Yamada, M. M. J. Bischoff, G. M. M. Heijnen, T. Mizoguchi and H. van Kempen, Observation of Spin-Polarized Surface States on Ultrathin Bct Mn(001) Films by Spin-Polarized Scanning Tunneling Spectroscopy, *Phys. Rev. Lett.*, 2003, **90**(5), 056803, DOI: 10.1103/PhysRevLett.90.056803.

86 J. Lobo-Checa, M. Matena, K. Müller, J. H. Dil, F. Meier, L. H. Gade, T. A. Jung and M. Stöhr, Band Formation from Coupled Quantum Dots Formed by a Nanoporous Network on a Copper Surface, *Science*, 2009, **325**(5938), 300–303, DOI: 10.1126/science.1175141.

87 M. F. Crommie, C. P. Lutz and D. M. Eigler, Confinement of Electrons to Quantum Corrals on a Metal Surface, *Science*, 1993, **262**(5131), 218–220, DOI: 10.1126/science.262.5131.218.

88 A. Winkelmann, C. Tusche, A. Akin Ünal, M. Ellguth, J. Henk and J. Kirschner, Analysis of the Electronic Structure of Copper via Two-Dimensional Photoelectron Momentum Distribution Patterns, *New J. Phys.*, 2012, **14**(4), 043009, DOI: 10.1088/1367-2630/14/4/043009.

89 R. Courths, H. Wern and S. Hüfner, The Tamm Surface State on Cu(111) and Ag(111), *Solid State Commun.*, 1987, **61**(4), 257–260, DOI: 10.1016/0038-1098(87)91014-3.